

Suzaku Observations of Abell 1795: Cluster Emission to R_{200}

Marshall W. BAUTZ, Eric D. MILLER

*Kavli Institute for Astrophysics & Space Research, Massachusetts Institute of Technology,
Cambridge, MA USA
mwb@space.mit.edu*

Jeremy S. SANDERS

Cambridge University, Cambridge, UK

Keith A. ARNAUD, Richard F. MUSHOTZKY, F. Scott PORTER
NASA's Goddard Space Flight Center, Greenbelt, MD USA

Kiyoshi HAYASHIDA

Osaka University, Osaka, Japan

J. Patrick HENRY

University of Hawaii, Honolulu, HI USA

John P. HUGHES

Rutgers University, New Brunswick, NJ USA

Madoka KAWAHARADA, Kazuo MAKASHIMA, Mitsuhiro SATO
University of Tokyo, Tokyo, Japan

and

Takayuki TAMURA

*Institute of Space and Astronautical Sciences, Japan Aerospace Exploration Agency,
Sagamihara, Japan*

(Received ; accepted)

Abstract

We report Suzaku observations of the galaxy cluster Abell 1795 that extend to $r_{200} \approx 2$ Mpc, the radius within which the mean cluster mass density is 200 times the cosmic critical density. These observations are the first to probe the state of the intracluster medium in this object at $r > 1.3$ Mpc. We sample two disjoint sectors in the cluster outskirts ($1.3 < r < 1.9$ Mpc) and detect X-ray emission in only one of them to a limiting (3σ) soft X-ray surface brightness of $B_{0.5-2 \text{ keV}} = 1.8 \times 10^{-12} \text{ erg s}^{-1} \text{ cm}^{-2} \text{ deg}^{-2}$, a level less than 20% of the cosmic X-ray background brightness. We trace the run of temperature with radius at $r > 0.4$ Mpc and find that it falls relatively rapidly ($T_{\text{deprojected}} \propto r^{-0.9}$), reaching a value about one third of its peak at the largest radius we can measure it. Assuming the intracluster medium is in hydrostatic equilibrium and is polytropic, we find a polytropic index of $\Gamma = 1.3^{+0.3}_{-0.2}$ and we estimate a mass of $4.1^{+0.5}_{-0.3} \times 10^{14} M_{\odot}$ within 1.3 Mpc, somewhat (2.7σ) lower than that reported by previous observers. However, our observations provide evidence for departure from hydrostatic equilibrium at radii as small as $r \sim 1.3 \text{ Mpc} \approx r_{500}$ in this apparently regular and symmetrical cluster.

Key words: galaxies:clusters:X-rays, galaxies:clusters:individual:Abell 1795

1. Introduction

Spatially resolved X-ray spectroscopy is essential for mapping the distribution of mass, intracluster plasma, and heavy elements in galaxy clusters. Although Chandra and XMM-Newton have provided a wealth of information on these quantities in the central regions of clusters, relatively little is known about their outer regions, at radii greater than $\sim 0.5r_{200}$. Here r_{200} is the radius within which the mean cluster density is 200 times the critical cosmic density. In the simplest case of the collapse of a spherical density perturbation in an Einstein-deSitter universe, it is expected that the dark and baryonic matter within r_{200} will have reached dynamical equilibrium (Evrard, Metzler & Navarro 1996). Cluster emission from

the vicinity of r_{200} is difficult to observe efficiently with Chandra and XMM-Newton because of their relatively high (and, in the latter case, time-variable) levels of instrumental background.

The study of cluster outskirts is important for several reasons. First, a direct X-ray measurement of total cluster mass (e.g., within r_{200}) requires knowledge of the ICM temperature profile at this radius. This is especially important to facilitate comparison between X-ray and weak-lensing mass profiles, as the latter are difficult to measure in the inner regions of clusters. Second, structure and cluster formation models make definite predictions about total mass and ICM distributions to these radii (Navarro, Frenk & White 1997; Borgani et al. 2004; Roncarelli et al. 2006), so measurements in this radial range offer a test of

these models. Finally, to the extent that r_{200} marks the approximate boundary of the dynamically relaxed region of a cluster, one might expect to find inhomogeneities in the ICM that could provide a direct view of the accretion processes by which clusters grow.

ROSAT has been used to characterize the X-ray surface brightness of the outer regions ($r \sim r_{200}$) of individual clusters (Vikhlinin, Forman & Jones 1999) and, using stacking techniques, of ensembles of objects (Neumann 2005). Chandra surface brightness profiles in the range $r_{500} < r < r_{200}$ for a sample of relatively distant clusters have been studied by Ettori & Balestra (2008). Recent Suzaku observations have successfully probed out to and beyond r_{200} for a handful of clusters (George et al. 2008; Fujita et al. 2008; Reiprich et al. 2008).

In this paper we present Suzaku measurements of the surface brightness and temperature of the intracluster medium of the X-ray luminous ($L_{X,bol} = 1.4 \times 10^{45}$ erg s $^{-1}$) cluster Abell 1795. This is a relatively hot (spatially-averaged $kT = 5.3$ keV) cluster with a cool core (Horner 2001; Vikhlinin et al. 2006; Snowden et al. 2008). Although Chandra shows a 40-arcsec-long ($50 h_{70}^{-1}$ kpc) plume “trailing” the brightest cluster galaxy (Fabian et al. 2001), outside of the very center the cluster is quite regular and appears relaxed. From the observed temperature, and scaling relations derived from simulations (Evrard, Metzler & Navarro 1996; Arnaud & Evrard 1999) we estimate $r_{500} = 1.3 h_{70}^{-1}$ Mpc, consistent with the Chandra measurements of Vikhlinin et al. (2006), and $r_{200} = 1.9 h_{70}^{-1}$ Mpc ($26'$) for our assumed cosmology¹. We exploit the relatively low and stable Suzaku background to trace the temperature and ICM density to the vicinity of r_{200} .

As noted by Bryan & Norman (1998), if the virial radius $r_{virial} = r_{\Delta_v}$ is derived from the collapse of a spherical top-hat density perturbation, assuming that the cluster has just virialized, then for an Einstein-deSitter cosmology $\Delta_v = 18\pi^2 \approx 180$, independent of redshift. In general, however, Δ_v is function of cosmology and redshift, and for our Λ CDM cosmology at the redshift of Abell 1795 $\Delta_v \approx 100$, so the virial radius is considerably larger than r_{200} . For Abell 1795 we expect $r_{100} \approx 1.35 r_{200}$. Here Δ_v is the ratio of the mean cluster mass density within r_{Δ_v} to the critical cosmic density.

2. Observations, Data Reduction & Analysis

2.1. Observations

Abell 1795 was observed on 2005 Dec 10, during the Suzaku performance verification phase, with a series of 5 overlapping pointings, illustrated in Figure 1. The results reported here were obtained with XIS (Koyama et al. 2007) data from version 2.0.6.13 of the Suzaku data processing pipeline. Data obtained with 3x3 and 5x5 editing modes for each pointing were merged and standard filters

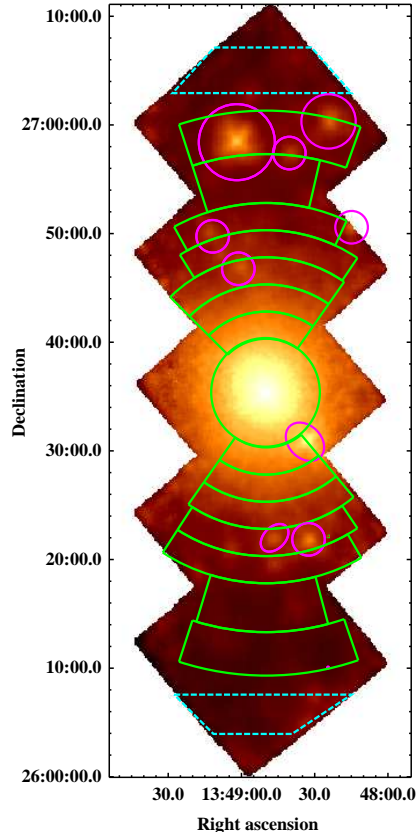


Fig. 1. Mosaic of five pointings (0.5-2 keV), with North at top and East at left. The image has been adaptively smoothed. Cluster spectra are taken from the solid green circle and annular sectors. Background regions are the dashed blue trapezoids. Magenta circles and ellipses surround excluded point sources.

(requiring earth elevation greater than 5 degrees, sunlit earth elevation angle greater than 20 degrees, cutoff rigidity greater than 6 GeV/c, and excluding data obtained during and just after passages through the South Atlantic Anomaly) were applied. Events in detector regions nominally illuminated by the XIS calibration sources were also excluded. The net good exposure times after filtering were 10.2 ks, 23.9 ks, 24.6 ks, 27.3 ks and 38.3 ks for the central, near-north, near-south, far-north and far-south pointings, respectively. Thus the total good exposure time was 124.3 ks.

Smoothed images of each field were inspected by eye and regions centered on nine obvious point sources were excluded, as indicated in Figure 1.

2.2. Image Analysis

To obtain a properly normalized cluster surface brightness profile from our multiple pointings, we used the following procedure to generate exposure maps. First, simulated monochromatic photon lists representing a uniform, $20'$ radius extended source were constructed, using 10^7 photons at a number of energies for each detector and pointing. The energy bins were selected to repre-

¹ We assume a flat, Λ CDM cosmology with $H_0 = 70$ km s $^{-1}$ Mpc $^{-1}$, $\Omega_M = 0.3$ and $\Omega_\Lambda = 0.7$. One arc minute corresponds to 73 kpc at the cluster redshift ($z = 0.063$) in this cosmology. Unless otherwise noted, quoted errors correspond to 90% confidence intervals.

sent roughly constant regions of the instrumental effective area curve. Each simulated photon list was used as input to the XRT ray-tracing simulator (`xissim`; Ishisaki et al. 2007), which includes the effects of the optical blocking filter (OBF) contamination, producing an image for each detector, pointing, and energy combination. To increase signal-to-noise, these flat field images were smoothed by a two dimensional Gaussian kernel with $72''$ FWHM. The calibration source regions and regions of low effective area near the chip edges were clipped. Spectral weights were determined from a spectral model fit to the cosmic X-ray background (described in Section 2.3.2 below). These spectral weights were chosen under the null hypothesis that surface brightness fluctuations in the cluster outskirts are due to cosmic background variations. When applied to cluster emission, they will result in an overestimate of the cluster surface brightness, however we estimate this to be less than 10% (5%) in the 0.5–2 keV (2–8 keV) range for the cluster temperatures and abundances measured in this work. Errors in surface brightness between cluster regions of different temperatures (ranging from 2–6 keV) will be less than 2% due to the spectral weighting. For each chip and pointing, the flat field frames were combined using the spectral weighting to produce an exposure map. Finally, the individual exposure maps were mosaicked onto a common sky coordinate (WCS) reference frame and summed.

Images from each pointing toward the cluster were extracted in the 0.5–2 keV and 2–8 keV bands, and these were mosaicked in sky coordinates. Cutoff-rigidity-weighted particle background rates were computed for each spectral band, sensor and pointing from the archive of ‘night-earth’ data (i.e., data obtained during orbit night while Suzaku pointed at the earth; Tawa et al. 2008). A (spatially uniform) particle background component was then subtracted from each cluster image, and each resulting image was then divided by the appropriate exposure map. The exposure-corrected, 0.5–2 keV mosaic image is shown in Figure 1. For purposes of this Figure, the background- and exposure-corrected image has been smoothed with an adaptive, circular kernel. The kernel radius is chosen to include at least 25 counts, up to a maximum radius of 10 binned pixels ($84''$).

2.3. Spectral Analysis and X-ray Background

2.3.1. Analysis and Cluster Modeling

Pulse-height spectra were accumulated for each in a series of annular sectors 2.5–4′ in width, depending on radius. The spectral extraction regions are illustrated in Figure 1. Two ancillary response functions (ARF files) were constructed for each region and XIS detector using the Monte Carlo FTOOL² `xissimarfgen` v2008-04-05 (Ishisaki et al. 2007). The first ARF was produced from a 20′ radius uniform surface brightness source; this response file was used to fit uniform background emission in the spectral analysis that follows. The second ARF was produced from the cluster surface brightness distribution results described in Section 4.1; this response

was used to fit cluster emission in each region. These files properly account for energy-dependent vignetting and scattering properties of the Suzaku XRT, as well as for the time-dependent contamination layer on each of the XIS optical blocking filters. Corresponding detector redistribution functions (RMF files) were constructed using the FTOOL `xisrmfgen` v2007-05-14. Cutoff-rigidity-weighted particle-induced background spectra were determined from night-earth data for each sensor and pointing using the FTOOL `xisnxbgen` v2008-03-08. These background spectra were subtracted from each source spectrum before fitting.

XSPEC v12.5.0 (Arnaud 1996) was used to fit data from all four XIS sensors simultaneously for all spectral fits reported here. Spectral fitting was confined to the 0.55–8 keV band where the response calibration is best. Calibration observations directly constrain the time-dependent, on-axis absorption by contamination of the XIS optical blocking filter in this spectral band (Koyama et al. 2007).

The emission from each cluster region was modelled by simultaneously fitting the pulse-height spectra from the cluster region and two background regions. The sum of a thin thermal plasma model (`mekal` in XSPEC) plus a cosmic background model (described in Section 2.3.2 below) was fit to each cluster spectrum, while only the background model was fit to the background regions. In all fits the cluster heavy element abundance, relative to cosmic values (Anders & Grevesse 1989), was allowed to vary. The best-fit redshift determined from the central 5′ region ($z = 0.0626 \pm 0.0008$) is consistent with the optical cluster redshift ($z = 0.0625 \pm 0.0003$) reported by Smith et al. (2004). The redshift was fixed at the optical value for other spectral fits. The combined XIS0,2,3 (FI) spectra and best-fit model components for the central 5′ and the northern extension are shown in Figure 2.

2.3.2. Cosmic Background Model

Spectra of the celestial X-ray background outside the cluster were obtained from two trapezoidal background regions at the northern and southern extremes of the observed field, 2.0 to 2.3 Mpc from the cluster center; see Figure 1. The background spectral model for each fit included the sum of absorbed power-law and soft thermal components, to account for extragalactic and Galactic backgrounds, respectively. When modelling the spectra of the faintest cluster regions (those with $r > 17.5'$) we also included a suite of emission lines to account for possible contributions from geocoronal solar wind charge exchange (SWCX). We find that the contribution of SWCX emission is uncertain and, though small, may be significant in the interpretation of the emission detected in these regions. In this section we describe the background model used for the brighter ($r < 17.5'$) cluster regions, for which SWCX is neglected. We discuss our treatment of SWCX emission in the cluster outskirts in the following section.

Best-fit spectral model parameters for the background regions, neglecting SWCX emission, are shown in the upper half of Table 1. Consistent results (within $\pm 6\%$ in normalization) were obtained for each model component

² <http://heasarc.gsfc.nasa.gov/ftools>

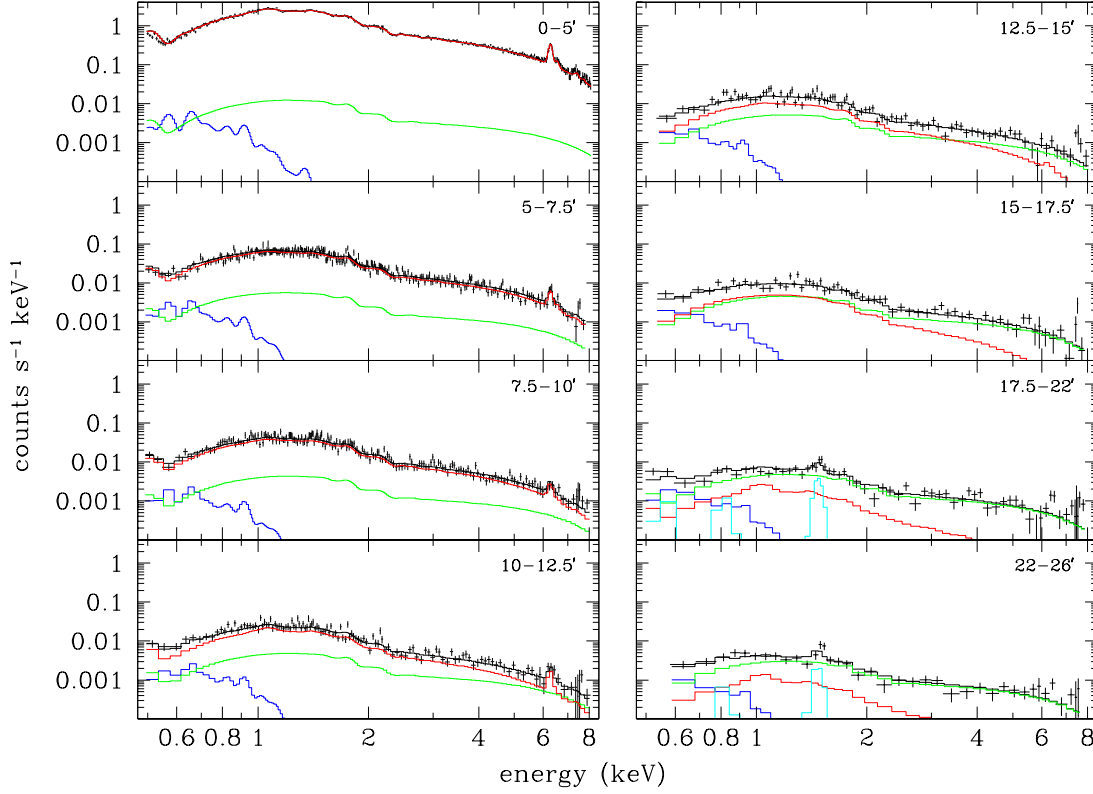


Fig. 2. Spectra of the central $5'$ radius region and annuli toward the north from Abell 1795. The locations of the regions are shown in Figure 1. For each region, the black points represent the combined count rate from the three FI devices (XIS0,2,3), while the solid lines show contributions from individual model components: the Galactic background (blue); the extragalactic background (green); the cluster (red); and solar wind charge exchange (cyan). The total model is given by the black line.

Table 1. Background Model Parameters^a

Component	North	South	Joint
without SWCX			
Power Law I_1^b keV	11.5 ^{+0.6} _{-0.7}	10.3 ^{+0.6} _{-0.6}	10.9 ^{+0.4} _{-0.4}
Thermal kT^c	0.15 ^{+0.03} _{-0.04}	0.19 ^{+0.04} _{-0.02}	0.18 ^{+0.02} _{-0.03}
Power Law B^d	7.7 ^{+0.4} _{-0.4}	7.0 ^{+0.4} _{-0.4}	7.3 ^{+0.3} _{-0.3}
Thermal B^d	2.9 ^{+0.7} _{-0.7}	3.0 ^{+0.7} _{-0.6}	3.0 ^{+0.5} _{-0.5}
Total B^d	10.6 ^{+0.7} _{-0.7}	10.0 ^{+0.7} _{-0.7}	10.3 ^{+0.5} _{-0.5}
with SWCX			
Power Law I_1^b keV	11.3 ^{+0.6} _{-0.7}	10.1 ^{+0.7} _{-0.7}	...
Thermal kT^c	0.18 ^e	0.18 ^e	...
Power Law B^d	7.6 ^{+0.4} _{-0.5}	6.8 ^{+0.5} _{-0.5}	...
Thermal $B^{d,f}$	2.8 ^{+1.3} _{-2.5}	2.8 ^{+1.1} _{-2.2}	...
SWCX $B^{d,f}$	1.5 ^{+2.9} _{-1.0}	1.3 ^{+2.3} _{-0.7}	...
Total B^d	11.9 ^{+0.7} _{-0.8}	11.2 ^{+0.7} _{-0.7}	...

Notes:

^a uncertainties are 90% confidence for 1 interesting parameter

^b intensity, $\text{ph s}^{-1} \text{cm}^{-2} \text{keV}^{-1} \text{sr}^{-1}$ at 1 keV; photon index fixed at $\Gamma = 1.4$

^c keV; abundance fixed at solar

^d surface brightness, $10^{-12} \text{erg s}^{-1} \text{cm}^{-2} \text{deg}^{-2}$, 0.5–2 keV

^e kT was fixed at 0.18 keV for the model including SWCX

^f the best-fit thermal and SWCX fluxes are anti-correlated

in the two background regions. Since our spectral analysis regions are quite small, expected Poisson fluctuations in the extragalactic background are actually larger than $\pm 6\%$, so this level of agreement must be regarded as fortuitous. To allow for these fluctuations, the normalization of the corresponding spectral component was allowed to vary separately when fitting each region of the cluster. This point is discussed in detail in Section 3.4 below.

The 2–10 keV surface brightness of the power-law component, determined from the joint fit to both the north and south background regions, is $B_{2-10} = 21.7 \pm 1.5 \times 10^{-12} \text{ erg s}^{-1} \text{ cm}^{-2} \text{ deg}^{-2}$, in excellent agreement with the value reported by DeLuca & Molendi (2004) from XMM-Newton observations ($22.4 \pm 1.6 \times 10^{-12} \text{ erg cm}^{-2} \text{ s}^{-1} \text{ deg}^{-2}$). As a check on the estimated 0.5–2 keV background, we determined the ROSAT All-Sky Survey (RASS) surface brightness in an annulus centered on Abell 1795 with inner and outer radii of 0.5 and 1 degree, respectively. We used the X-ray Background Tool³ (Snowden et al. 1997) provided by NASA’s Goddard Space Flight Center to extract the ROSAT spectrum for this region. We then fit the recommended X-ray background model (Kuntz & Snowden 2000), which includes two soft thermal components and a power law, to the ROSAT spectrum in the 0.1–2 keV band. This yields a surface brightness in the 0.5–2 keV band of $B_{0.5-2} = 11.1^{+2}_{-3} \times 10^{-12} \text{ erg s}^{-1} \text{ cm}^{-2} \text{ deg}^{-2}$, in excellent agreement with our (more precise) Suzaku estimates listed in Table 1.

Thus, even ignoring possible contributions of SWCX emission, our Suzaku background estimates are in excellent agreement with previous measurements of both the Galactic and extragalactic components. In our chosen spectral bands we can determine background (and foreground) flux in the vicinity of Abell 1795 with a relative statistical uncertainty of just over 5%. As we discuss in section 3.4 below, the accuracy of our background subtraction is in fact limited by cosmic variations in the density of unresolved background sources rather than by statistical or instrumental systematic errors.

2.3.3. Solar Wind Charge Exchange Model

Heavy ions in the solar wind undergo charge exchange with neutral atoms in the Earth’s geocorona and in the solar magnetosphere, resulting in a field-filling emission line spectrum which contaminates the more distant cluster emission. Lines typically produced by solar wind charge exchange (SWCX) include those of highly-ionized C, O, Ne, and Mg (e.g., Snowden et al. 2004; Fujimoto et al. 2007). Variations in the solar wind can produce variations in the geocoronal SWCX flux on timescales of seconds, while heliospheric SWCX contributes a stable or slowly-varying X-ray background (e.g., Cravens 2000).

We have checked for SWCX variability by constructing light curves for each pointing, excluding the center pointing where the cluster emission is expected to dominate any SWCX emission. Light curves were extracted for all four XIS detectors in the 0.4–2 keV range from the full detector field, excluding point sources. Particle background

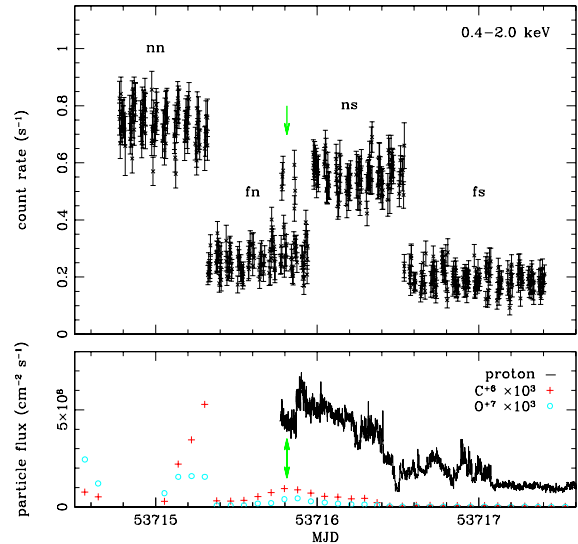


Fig. 3. (top) Combined, background-subtracted light curve for all detectors in the 0.4–2 keV range. The four outer pointings are shown (nn: near north; fn: far north; ns: near south; fs: far south). (bottom) Solar wind ion flux from the ACE satellite, corrected for travel time to the Earth. Count rate variation and significant enhancements in the solar proton and ion flux indicate possible SWCX contamination. The green arrows indicate a strong count rate flare.

light curves were constructed from the ‘night-earth’ data archive (Tawa et al. 2008) using the appropriate cut-off rigidity time series, and these were subtracted from the individual detector light curves, which were then combined for each field. The resultant complete light curve is shown in the top panel of Figure 3. Any residual variations in count rate are a result of variations in the emission from the Galactic foreground, the unresolved extragalactic background, the cluster, and/or SWCX. The extraction regions for corresponding pointings are identical in sky coordinates, so any differences between far north and far south (“fn” and “fs”) or between near north and near south (“nn” and “ns”) must be due to variations (temporal or spatial) in the surface brightness of these emission components.

There is clear variability in the light curve. Most notably, the far north count rate shows a strong spike (marked by the green arrow). Count rates in the other three pointings are also inconsistent with the null hypothesis of constancy (p-values $\lesssim 0.1$), although they lack strong variation. Analysis of public data from the Advanced Composition Explorer (ACE) satellite (Stone et al. 1998) reveals an enhanced flux of protons and heavy ions during much of the observation (see Figure 3, bottom panel). Although there are gaps in the ACE data, the proton, C^{+6} , and O^{+7} flux during the far north and near north pointings (near MJD 53716) are similar to levels observed during times of SWCX contamination in a Suzaku observation of the North Ecliptic Pole (Fujimoto et al. 2007). The far north count rate spike occurs near a

³ <http://heasarc.gsfc.nasa.gov/cgi-bin/Tools/xraybg/xraybg.pl>

Table 2. Modeled SWCX Emission Lines

transition	energy (keV)	photon flux (ph s ⁻¹ cm ⁻² sr ⁻¹)	
		North	South
O VII triplet	0.574	3.03 ^{+4.07} _{-1.56}	< 6.66
O VIII Ly α	0.654	< 2.25	< 1.77
O VIII Ly β	0.774	< 0.71	< 0.61
O VIII Ly γ	0.817	< 0.63	0.49 ^{+0.50} _{-0.43}
Ne IX triplet	0.923	< 0.47	0.46 ^{+0.38} _{-0.35}
Ne X Ly α	1.022	< 0.31	0.41 ^{+0.28} _{-0.27}
Mg XI triplet	1.345	< 0.11	< 0.23
Mg XII Ly α	1.472	0.43 ^{+0.23} _{-0.22}	< 0.16
Mg XII Ly β	1.745	< 0.08	< 0.11

peak in both the proton and heavy ion flux. There is an additional spike in the heavy ion flux near the end of the near north observation. The solar particle flux near the end of the observations (after MJD 53716.5) is consistent with that observed during quiescence in other Suzaku observations (Fujimoto et al. 2007; Miller et al. 2008). We conclude that our observations are likely contaminated by variable SWCX emission.

We estimate the level and variability of geocoronal SWCX contamination by comparing the emission from the (presumed cluster-free) background regions. As in Section 2.3.2 above, the non-SWCX background is modeled as the sum of a soft thermal (Galactic) background component and a power-law (extragalactic) component. When fitting the spectra of the relatively small background regions alone, we found strong degeneracies between the SWCX and thermal model parameters, so we fixed the temperature of the thermal model at $kT = 0.18$ keV, the value determined from the joint SWCX-free model. The photon index of the power-law component was fixed at $\Gamma = 1.4$. The normalizations of both background components were allowed to vary independently in each region (see Section 3.4).

To model the SWCX in the background regions, we include a suite of unresolved Gaussian emission lines typically observed in SWCX emission between 0.5–2 keV (Snowden et al. 2004; Fujimoto et al. 2007), listed in Table 2. The line energies are fixed to their theoretical values, using the energy of the dominant forbidden transition for helium-like lines of O VII, Ne IX, and Mg XI (Koutroumpa et al. 2007). The line fluxes are allowed to vary independently.

We use Markov chain Monte Carlo (MCMC) techniques to constrain the relatively large number of model parameters and their uncertainties. The MCMC tools in XSPEC v12.5.0 (Arnaud 1996) were used to produce 8 chains of 7000 steps, of which the first 2000 were excluded as “burn-in”. The input covariance matrix was scaled to get sufficient mixing (i.e., so that the fraction of repeated locations in parameter space was ~ 0.8). These 40,000 chain steps were combined to produce probability distributions for each of the 22 free parameters, and from these the best fit value and 90% confidence intervals were estimated.

Both the far north and far south background regions show an excess of line emission above the Galactic and extragalactic components. The spectra in Figure 4 suggest enhancement of the O VII triplet near 0.56 keV (evident in XIS1) and a $\sim 3\text{-}\sigma$ feature near 1.5 keV (evident in XIS0,2,3) in the far north spectrum. The latter is consistent with Mg XII Ly α . The far south spectra show much weaker upper limits to the enhancement near 0.56 keV (in XIS1) and 1.5 keV (in XIS0,2,3), but they contain excess emission in the 0.9–1.0 keV region (evident in all detectors) that is consistent with Ne IX and Ne X. The line strengths and upper limits are shown in Table 2. The Mg XII line is similar in energy to a strong instrumental Al K α line, however the Al K α line flux would have to be enhanced by more than a factor of 3 during the full far north exposure to produce such strong residual emission. Background variations of this sort have not been reported in previous Suzaku observations, nor in the night-earth background analysis of Tawa et al. (2008). The presence of a Mg XII SWCX line without additional SWCX lines such as O VIII, Ne IX and Ne X seems puzzling, although since detection of Mg XII with XMM-Newton is complicated by a much stronger and more variable instrumental Al K α line, there are few data from other sources. Mg XII Ly γ has likely been observed in another XMM-Newton SWCX event (Carter & Sembay 2008). Snowden et al. (2004) claim a Mg XI SWCX detection at 1.34 keV. The upper limits on the photon fluxes for other expected lines are low compared to other SWCX detections, which suggests that our observations are less affected by geocoronal SWCX.

The contributions of SWCX and other model components to the total surface brightness in the background regions are listed in the lower half of Table 1. The Table shows that SWCX emission is detected at better than 90% confidence during our observations of both far north and far south fields, and that the SWCX emission spectrum differs significantly between the two observations. However, in each field SWCX contributes less than 15% of the total, soft-band cosmic background brightness, and the difference between SWCX contributions to the two fields is less than 5% of the total cosmic background brightness.

Our spectral analysis of the outermost regions of the cluster ($r > 17.5'$) follows that used for the interior of the cluster, except that we include the SWCX model described above in the background model (see Figure 2). In particular, the soft thermal (Galactic) background component was fit with a single free temperature and normalization for all regions (17.5–26' north and south, and the north and south background regions). The power-law (extragalactic) background component was fit with a fixed photon index $\Gamma = 1.4$ and normalizations that were allowed to vary independently in each region (see Section 3.4). A mekal component, with temperature, abundance, and normalization free to vary, was used to model cluster emission.

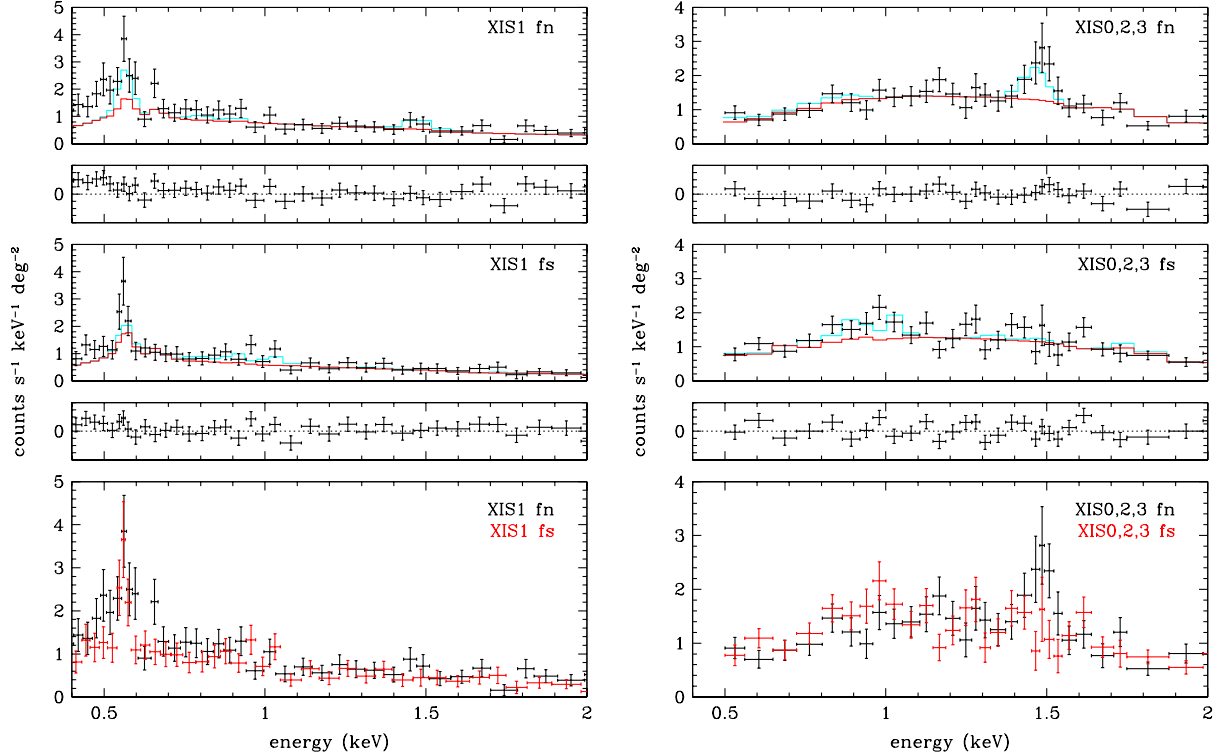


Fig. 4. Spectra of the two background regions from the BI detector XIS1 (left) and the combined FI detectors XIS0,2,3 (right). The labels “fn” and “fs” refer to the far north and far south pointings, respectively. In the top panels, the red lines indicate the best-fit diffuse Galactic + extragalactic background, and the cyan lines indicate 90% upper limits to SWCX emission modeled by Gaussian lines (see Table 2). The residuals are calculated from the combined background + SWCX model. The model was fit simultaneously to spectra from the four detectors; the FI spectra were only combined here to improve the displayed S/N. The bottom panels directly compare the counts spectra from the far north (black) and far south (red) background regions. Differences can be seen near the O VII (0.56 keV), Ne IX and Ne X (1 keV), and Mg XII (1.5 keV) lines.

3. Systematic Errors

We wish to measure cluster emission at very low surface brightness levels and it is important to understand the influence of various instrumental and other systematic effects that may limit our ability to do so. In this section we consider a number of potential systematic errors in more detail, including i) the impact of our choice of passband on temperature measurement accuracy; ii) the accuracy of our knowledge of spatial response variations over the XIS field of view; iii) the impact of scattered light, both from the bright cluster core and from point sources in the field of view, on the accuracy of our spectral modelling; and iv) the effects of counting statistics on the flux of unresolved sources.

3.1. Spectral passband, Galactic absorption and cluster temperature

A drawback of our decision to ignore data at energies below 0.55 keV in our spectral fits is that it is difficult to constrain the Galactic absorption directly from the X-ray data unless the signal-to-noise ratio is quite high. On the other hand, we have found that the best-fit model

temperature and Galactic column do exhibit a mild (anti) correlation. Thus, any systematic errors in determination of the Galactic column (such as might arise from spatially varying errors in the contamination correction) can induce errors in the measured temperature. We have therefore elected to fix the model Galactic column density at the value obtained by fitting to the high-signal-to-noise ratio spectrum of the integrated cluster emission at $r < 5.0'$. Fitting results are shown in Table 3. The best-fit value of n_H is in excellent agreement with the nominal Galactic column ($n_H = 1.2 \times 10^{20} \text{ cm}^{-2}$) estimated for this field by NASA’s HEARSARC tool `nH`.⁴

3.2. Spatial response variations and reproducibility of spectral modelling

As a check on the reliability of the Suzaku calibration, we compared fitting results for regions of the cluster observed with multiple pointings. Two such ‘overlap’ regions provide sufficient flux for a meaningful comparison. Each

⁴ <http://heasarc/gsfsc.nasa.gov/cgi-bin/Tools/w3nh>. The column densities estimated from the Leiden/Argentine/Bonn (Kalberla et al. 2005) and Dickey & Lockman (1990) maps agree within 1%.

Table 3. Best-fit Model Parameters for $r < 5.0'$

Flux ^a	kT ^b	Abundance	n_H ^c	χ^2/DOF
$7.46^{+0.04}_{-0.03}$	5.26 ± 0.06	0.360 ± 0.018	1.2 ± 0.3	4709.6/4481

Notes:

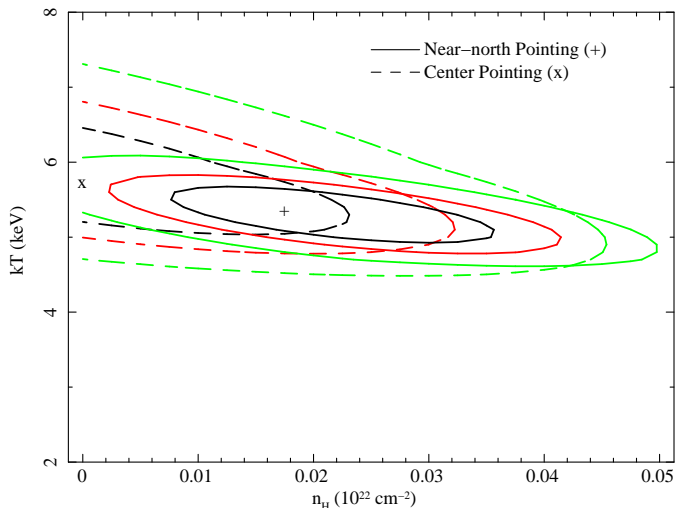
^a 10^{-11} erg s⁻¹ cm⁻², 0.55–8 keV; ^b keV; ^c 10^{20} cm⁻²

Fig. 5. Contours of χ^2 over the n_H - kT plane derived from two distinct observations of region of Abell 1795. The region in question is an annular sector $5'$ – $7.5'$ north of the cluster. Contours at 68% (black), 90% (red) and 95% (green) confidence from the ‘near-north’ (solid contours) and ‘center’ (dashed contours) pointings are indicated. The cross and x symbols indicate the best fit values for these two regions, respectively. The good agreement of these measurements from opposite sides of the XIS field of view illustrates the accuracy with which spatial response variations have been calibrated.

region is an annular sector with inner and outer radii of $5.0'$ and $7.5'$, respectively. The northern overlap region was observed with central and ‘near-north’ pointings; the southern overlap region was observed with the central and ‘near-south’ pointings. Thus each overlap region was observed on opposite sides of the XIS field of view. In order to gauge errors in the calibration of the soft response, we allowed the Galactic column to vary when fitting individual spectra. For each overlap region, the best-fit model parameters from the two pointings are consistent with one another within 90% confidence statistical errors ($\delta kT = 0.3$ keV). The level of agreement, as well as the magnitude of calibration errors, is illustrated in Figure 5, which shows contours of χ^2 in the n_H - kT plane for the northern overlap region. Figure 5 suggests residual systematic errors in the determination of the absorbing column may be of order $\delta n_H \sim 1 \times 10^{20}$ cm⁻². As noted above, in subsequent analysis we fix $n_H = 1.2 \times 10^{20}$ cm⁻² and include a systematic temperature error of $\delta kT = 0.15$ keV to account for this effect.

3.3. Scattered X-ray flux

We estimated the effect of X-rays scattered by the XRT from the bright, cool core of Abell 1795 to the

cluster outskirts with the aid of a number of simulations. For this purpose we used the FTOOLS `xissim` and `xissimarfgn` (Ishisaki et al. 2007). For fields centered $20'$ from a bright source (comparable to our far north and far south fields), actual stray intensity levels are expected to be less than ~ 2 times the values predicted by these tools (Serlemitsos et al. 2007).

To gauge the effect of scattered X-rays from the bright cluster core on the surface brightness profiles at large radius, we simulated observations of a point source located at the cluster center with a spectrum and total flux observed within $5'$ of the center (see Table 3). Since the actual cluster emission is more diffuse than assumed in this model, our simulation overestimates the scattered flux from the (unresolved) bright cool core of the cluster. We simulated the full mosaic observation of five pointings for each sensor, and normalized the simulated observations using the exposure maps discussed in Section 2.2 above. We then extracted surface brightness profiles for this point source using the same methods we used to extract the cluster profiles (as discussed in Section 4.1). In particular, all regions excluded from the cluster profiles because they contained cosmic sources were also excluded in the simulations. For clarity, we did not add a cosmic X-ray background signal to the simulated point source profile.

The resulting point-source surface brightness profile in the 0.5–2 keV band is shown by the points in Figure 6. The Figure shows that the expected scattered flux at $r > 10'$ exhibits a distinct oscillation at relatively low amplitude. The oscillation is presumably due to the variations with field angle of the intensity of so-called ‘secondary’ (single bounce) and ‘backside’ (three-bounce) reflections (Serlemitsos et al. 2007).

Comparison of Figure 6 with the estimated celestial background brightness listed in Table 1 shows that the surface brightness due to scattered flux in this radial range is always less than 7% of the cosmic background surface brightness we observe at the largest radii ($r > 30'$). The actual scattered intensity from the cluster will be below that shown in Figure 6 at these radii because convolution of the point response function (PRF) with the extended cluster flux distribution will reduce the amplitude of the oscillating wings. Serlemitsos et al. (2007) note that, given alignment tolerances of the XRT reflectors and pre-collimator blades, the actual scattered flux at $r = 20'$ could in principle exceed the ray-tracing simulations (which assume perfect alignment) by as much as a factor of 2. Allowing for this uncertainty, we expect that scattered cluster flux will contribute at most 10% of the total observed brightness at $r > 10'$.

We confirmed the effect of scattered cluster flux on

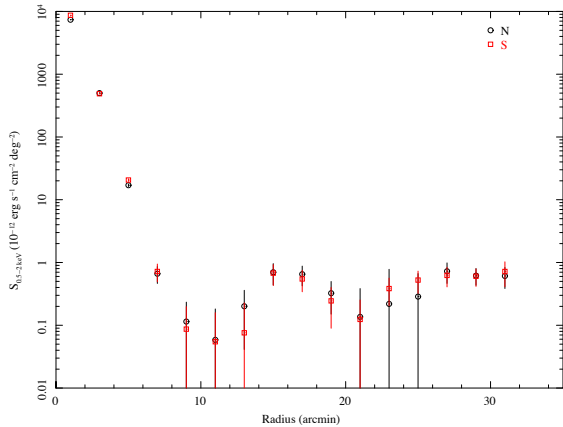


Fig. 6. Simulated surface brightness (points) in the 0.5–2 keV band for a point source located at the cluster center with flux equal to that from within $r < 5'$ of the cluster center. Surface brightness northward (black circles) and southward (red squares) from the source location are shown. No cosmic background has been added.

our spectral analysis in the outermost regions of our field ($17.5' < r < 32'$) by computing the effective area (as a function of energy) for detection of photons there originating from the central $5'$ of the cluster. Here we used the measured cluster surface brightness distribution as input to the effective area calculation, rather than a simple point source. Note that this central region produces more than 80% of the total cluster flux reported for A1795 in the Northern ROSAT All-Sky Survey (NORAS) catalog (Böhringer et al. 2000). Using these effective area functions, and the cluster spectral model described in Table 3, we employed XSPEC to simulate the flux and spectrum of X-rays scattered from the cluster center into each cluster (and background) region at $r > 17.5'$. The resulting fluxes are listed in the first two columns of Table 4.

We conclude from Table 4 that the scattered intensity from the cluster core contributes ~ 3 –5% of the total observed surface brightness in the regions for which we perform spectroscopy. Both magnitude and variation with radius are in agreement with the foregoing analysis of the PRF. We reiterate that uncertainties in collimator alignment render these estimates uncertain by as much as a factor of 2. The estimated scattered fluxes in the northern and southern regions differ somewhat, particularly in the radial range 17.5 – $22'$. The differences are presumably due to the exclusion of point sources in the north (see Figure 1), which changes the effective radii of the annular bins there, coupled with the rapidly varying scattered flux in this region (see Figure 6). In any event, the scattered flux in all regions listed in Table 4 is comparable to or less than the statistical errors in the estimated background (see Table 1). We note that, because of the oscillating PRF wings (see Figure 6), the simulations imply that spatial non-uniformity of the scattered flux will cause us to over-estimate the background at $r > 27.5'$, and thus to

(slightly) underestimate the cluster flux in the outer-most regions.

Finally, we investigated the effect of scattered flux from bright point sources on our cluster spectrophotometry. The brightest such source is in the far-north field, with Suzaku position⁵ $\alpha = 13\text{h}49\text{m}03.0\text{s}$, $\delta = +26^\circ 58' 46.1''$, and we estimate its flux to be $4.0 \pm 1.9 \times 10^{-13} \text{ erg s}^{-1} \text{ cm}^{-2}$ (0.5–2 keV) within an aperture of $2.5'$ radius. We have excluded a $3.5'$ diameter region around this source from the cluster analysis. We estimated the flux contributed by this source to each of our spectroscopic regions following methods described above for the cluster flux. Results are listed in Table 4. The wings of the image of this bright point source contribute less than 5% of the observed total flux to each of the two outermost spectral analysis regions (extending from $17.5'$ to $26'$ from the cluster). Thus in these two regions, the bright point source contribution is comparable to that from scattered cluster flux. In all other regions, the bright point source contribution is smaller. We note that point source contributions should be known more accurately than those from the cluster core because the ray-tracing simulations are better calibrated at $r \sim 3$ – $10'$ than at $r > 20'$ (Serlemitsos et al. 2007).

3.4. Cosmic background variations

Wide and deep X-ray surveys conducted over the past ~ 15 years have revealed a great deal about the distribution in flux and space of the sources that constitute the extragalactic X-ray background (Brandt & Hasinger 2005 and references therein). We have used this information to estimate the expected variation of the extragalactic background not resolved by Suzaku. On scales larger than the Suzaku PRF ($\sim 2'$), the correlation of source angular positions is weak (Yang et al. 2003), and for purposes of estimating the expected variance in our background, we neglect it. Formally the expected background surface brightness B due to sources with flux $S < S_{excl}$ is $B = \int_0^{S_{excl}} \frac{dN}{dS} S dS$, where $\frac{dN}{dS}$ is the differential number of sources per unit solid angle and flux. The expected variance of the background brightness, σ_B^2 , when measured over a solid angle Ω , is $\sigma_B^2 = (\int_0^{S_{excl}} \frac{dN}{dS} S^2 dS) / \Omega$. We adopt a broken power-law model for $\frac{dN}{dS}$ using parameters derived by Moretti et al. (2003).

It may be instructive to note that if the integral number counts $N(S > S_{excl})$ varied simply as $N(S > S_{excl}) \propto S_{excl}^{-\alpha}$, then the relative fluctuation in the unresolved background within a solid angle Ω would satisfy $\sigma_B/B = K(\alpha)/(N(S > S_{excl})\Omega)^{1/2}$, where the factor $K(\alpha)$ varies between $\sim 1/2$ and $3/2$ for appropriate values of α . This relationship sets the flux limit S_{excl} to which point sources must be detected for accurate background estimation in a field of solid angle Ω .

Our Suzaku data alone allow us to detect point sources to a limiting flux $S > S_{excl} = 10 S_{14}$, where S_{14} is the flux in units of $10^{-14} \text{ erg s}^{-1} \text{ cm}^{-2}$, in either the soft (0.5–2 keV) or hard (2–8 keV) bands. For a significant fraction of our

⁵ This source is coincident, within expected Suzaku position error of up to 20 arcsec, with 1RXS J134903.6+265845.

Table 4. Estimated scattered flux

Region ^a	From Cluster Core		From N. Point Source		Total	
	$B_{sc,0.5-2}^b$	$B_{sc,2-8}^b$	$B_{sc,0.5-2}^b$	$B_{sc,2-8}^b$	$B_{sc,0.5-2}^b$	$B_{sc,2-8}^b$
17.5–22 (N)	0.36	0.25	0.38	0.02	0.74	0.27
17.5–22 (S)	0.21	0.16	0.21	0.16
22–26 (N)	0.37	0.33	0.45	0.03	0.82	0.36
22–26 (S)	0.37	0.36	0.37	0.36
27.5–31.7 (N)	0.47	0.35	0.47	0.35
27.5–31.7 (S)	0.45	0.34	0.45	0.34

Notes:

^a Minimum and maximum radii, arcmin, north (N) or south (S) of cluster center.^b 10^{-12} erg s⁻¹ cm⁻² deg⁻², 0.5–2 and 2–8 keV

field, we can also use archival XMM-Newton observations to constrain the number of unresolved sources contributing to the Suzaku background at fluxes as low as $S_{excl} = 1.5S_{14}$ in the soft band, and $S_{excl} = 1.3S_{14}$ in the hard band (see below). Using our adopted source-count flux relation, we find the expected RMS fluctuations in background due to unresolved sources are $\sigma_B = 3.9(0.94) \times 10^{-12} \Omega_{0.01}^{-1/2}$ erg s⁻¹ cm⁻² deg⁻² for $S_{excl} = 10(1)S_{14}$ in the soft band. The corresponding fluctuation amplitudes in the hard band are $\sigma_B = 4.5(2.5) \times 10^{-12} \Omega_{0.01}^{-1/2}$ erg s⁻¹ cm⁻² deg⁻² for $S_{excl} = 10(1.3)S_{14}$. Here $\Omega_{0.01}$ is the solid angle of the measurement region in units of 10^{-2} deg².

The field coverage of the available XMM-Newton observations is shown in Figure 7. We searched the Second XMM-Newton Serendipitous Sky Survey (XMM2P) catalog available at NASA’s High Energy Astrophysics Science Archive Research Center⁶ for sources in our Suzaku field at distance $10' < r < 26'$ from the cluster center. We found that the effective (EPIC PN) exposure in this region ranges from 10–50 ksec. Our adopted XMM-Newton flux thresholds ($S_{excl} = 1.5S_{14}$ and $S_{excl} = 1.3S_{14}$ in the soft and hard bands, respectively) exceed the nominal XMM-Newton 5σ detection thresholds (Watson et al. 2001) for the minimum effective exposure available in our field. We summed the flux of sources brighter than these thresholds in each of our spectral analysis regions. Since the XMM2P catalog does not tabulate source flux in the 2–8 keV band, we estimated the 2–8 keV flux by scaling the tabulated XMM-Newton 2–12 keV flux by a factor appropriate for power-law photon number distribution with index 1.4 (that is, we assumed $S_{2-8} = S_{2-12} \times 0.67$.) The contributions of sources resolved by XMM-Newton to the Suzaku background, as well as the estimated fluctuations in the background due to fainter sources, are listed in Table 5.

In the outskirts of the cluster ($r > 10'$), the expected fluctuations in the unresolved background are $\approx 10^{-12}$ erg s⁻¹ cm⁻² deg⁻² (0.5–2 keV), or about 10% of the total (Galactic plus extragalactic) background. In our two background regions at $r > 27.5'$, which lack complete

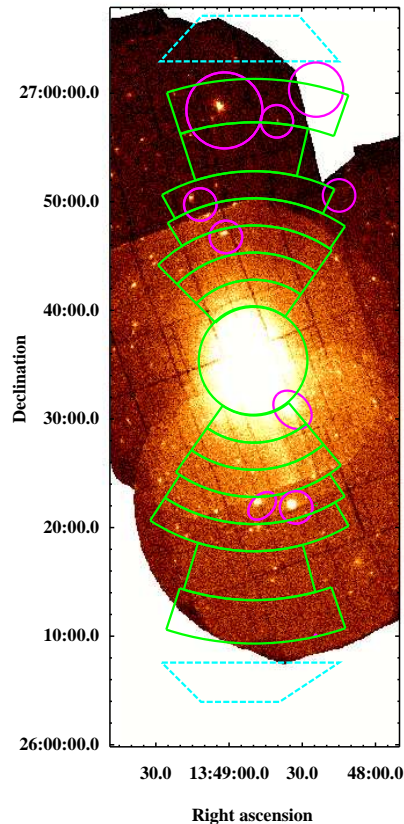


Fig. 7. XMM-Newton image of Abell 1795 field with Suzaku spectral analysis regions superposed in green. Where available, the XMM-Newton data constrain the background uncertainties due to point sources unresolved by Suzaku. As in Figure 1, background regions are the dashed blue trapezoids and magenta circles and ellipses show point sources excluded from the Suzaku data.

⁶ <http://heasarc.nasa.gov/>

Table 5. Estimated Background Contributions from Point Sources

Radius ^a	$\Omega_{0.01}^b$	0.5–2 keV				2–8 keV			
		S_{excl}^c	B_{res}^d	B_{unres}^d	σ_{unres}^d	S_{excl}^e	B_{res}^f	B_{unres}^f	σ_{unres}^f
North:									
5–7.5	0.60	10	0 ^g	7.8	4.9	10	0 ^g	16.4	5.8
7.5–10	0.85	10	0 ^g	7.8	4.2	10	0 ^g	16.4	4.9
10–12.5	0.93	1	2.2	3.1	0.96	1.3	2.7	12.0	2.6
12.5–15	0.98	1	3.9	3.1	0.94	1.3	3.8	12.0	2.6
15–17.5	0.91	1	1.3	3.1	0.98	1.3	0.	12.0	2.6
17.5–26	1.58	1	0	3.1	0.74	1.3	7.4	12.0	0.8
27.5–31.7	1.54	10	0 ^g	7.8	3.1	10	0 ^g	16.4	3.6
South:									
5–7.5	0.57	10	0 ^g	7.8	5.1	10	0 ^g	16.4	6.0
7.5–10	0.79	10	0 ^g	7.8	4.3	10	0 ^g	16.4	5.1
10–12.5	0.93	1	0	3.1	0.96	1.3	0	12.0	2.6
12.5–15	0.83	1	1.3	3.1	1.0	1.3	4.6	12.0	2.7
15–17.5	1.22	1	2.0	3.1	0.84	1.3	3.8	12.0	2.3
17.5–26	3.11	1	0	3.1	0.54	1.3	1.1	12.0	1.4
27.5–31.7	1.25	10	0 ^g	7.8	3.5	10	0 ^g	16.4	2.2

Notes:

^a Radial range of region relative to cluster center, arcmin; ^b Region solid angle, 10^{-2} deg²; ^c Limiting flux for resolved sources, in units 10^{-14} ergs s⁻¹ cm⁻², 0.5–2 keV; ^d 10^{-12} ergs s⁻¹ cm⁻² deg⁻², 0.5–2 keV; ^e Limiting flux for resolved sources, in units 10^{-14} ergs s⁻¹ cm⁻², 2–8 keV; ^f 10^{-12} ergs s⁻¹ cm⁻² deg⁻², 2–8 keV; ^g These regions lack useful XMM-Newton coverage.

XMM-Newton coverage, the expected fluctuations are significantly larger, ranging from $3\text{--}3.5 \times 10^{-12}$ erg s⁻¹ cm⁻² deg⁻². We note also that the expected extragalactic background brightness for these regions is in excellent agreement with the measured values (see Table 1).

Finally, we stress that the expectation value of the extragalactic background brightness varies from region to region because the extragalactic source population (as well as our knowledge of it) varies (see Table 5). Thus, for example, it is appropriate when modelling the background to allow the extragalactic component to vary in brightness from region to region, and we do so in our fits.

4. Results and Discussion

4.1. Surface Brightness

Radial surface brightness profiles were extracted from exposure-corrected images in the 0.5–2 keV and 2–8 keV spectral bands using the Chandra X-ray Center’s CIAO/Sherpa tools. Point sources indicated in Figure 1 were excluded. The center of the profile was determined from a fit of a circular beta-model ($S(r) \sim (1+x^2)^{-(3\beta-\frac{1}{2})}$ with $x = \frac{r}{r_c}$) to the (two-dimensional) 0.5–2 keV image. A one-dimensional model consisting of a β -model plus a constant background was then fit to each of the radial profiles. The profiles and the best-fitting models are presented in Figure 8. The count-rate to flux conversions for these profiles were derived from the SWCX-free spectral model of the emission from the background regions (see the upper panel of Table 1). As explained in Section 2.2, this leads to a cluster flux overestimate of less than 10% (5%) for the 0.5–2 keV (2–8 keV) band. It is appropriate

for our null hypothesis that surface brightness variations in the A1795 outskirts are due to cosmic background fluctuations.

The northern and southern surface brightness profiles shown in Figure 8 agree remarkably well with one another (and with a simple β -model with $\beta = 0.64 \pm 0.01$) for $r < 1.0$ Mpc ($14'$) $\approx r_{2500}$. As expected, the cluster is symmetrical and evidently relaxed in this region. At larger radii, the profiles diverge, with the surface brightness apparently falling more rapidly than the β -model in the south, but actually rising in the north to an apparent peak near $r = 1.9$ Mpc ($26'$) $= r_{200}$ in the 0.5–2 keV band. The surface brightness in this peak is about twice that in the nominal background regions, which are at $r > 2.0$ Mpc ($r > 27.5'$). The southern profile actually drops $\sim 20\%$ below the level in the nominal background regions.

The surface brightness profiles at radii $r > 10'$ are re-plotted in Figure 9, along with estimates of the cosmic X-ray background as a function of radius. To minimize the Poisson fluctuations in the extragalactic background we have re-binned the data at $r > 18'$. The background estimates, shown as dashed histograms in Figure 9, include three components. We assume a spatially uniform Galactic contribution in the 0.5–2 keV band, with flux equal to the mean thermal flux obtained from the spectral fitting of the background regions (see Table 1): $B_{Gal} = 3.0 \pm 0.3 \times 10^{-12}$ erg s⁻¹ cm⁻² deg⁻² (1σ errors). This estimate assumes no SWCX emission; we consider the effects of SWCX below. We adopt as the extragalactic background the sum of the total flux of any point sources detected by XMM-Newton plus an estimate of the unresolved flux derived from our adopted model of number

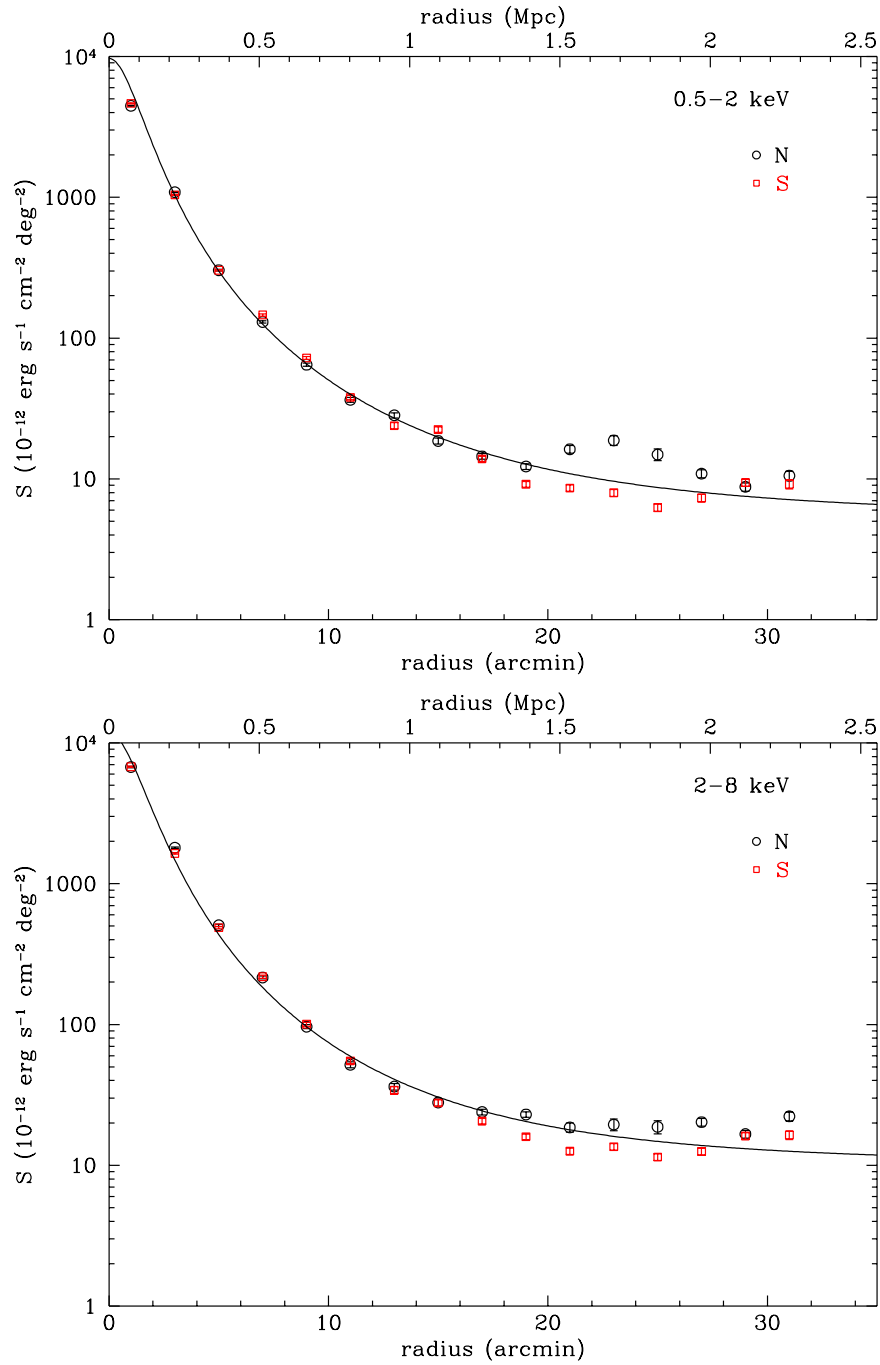


Fig. 8. Surface brightness profiles northward (black circles) and southward (red squares) from the cluster center in the 0.5–2 keV (upper panel) and 2–8 keV (lower panel) bands. The solid curves show the best-fit β -models to all the points (northward and southward) in each panel.

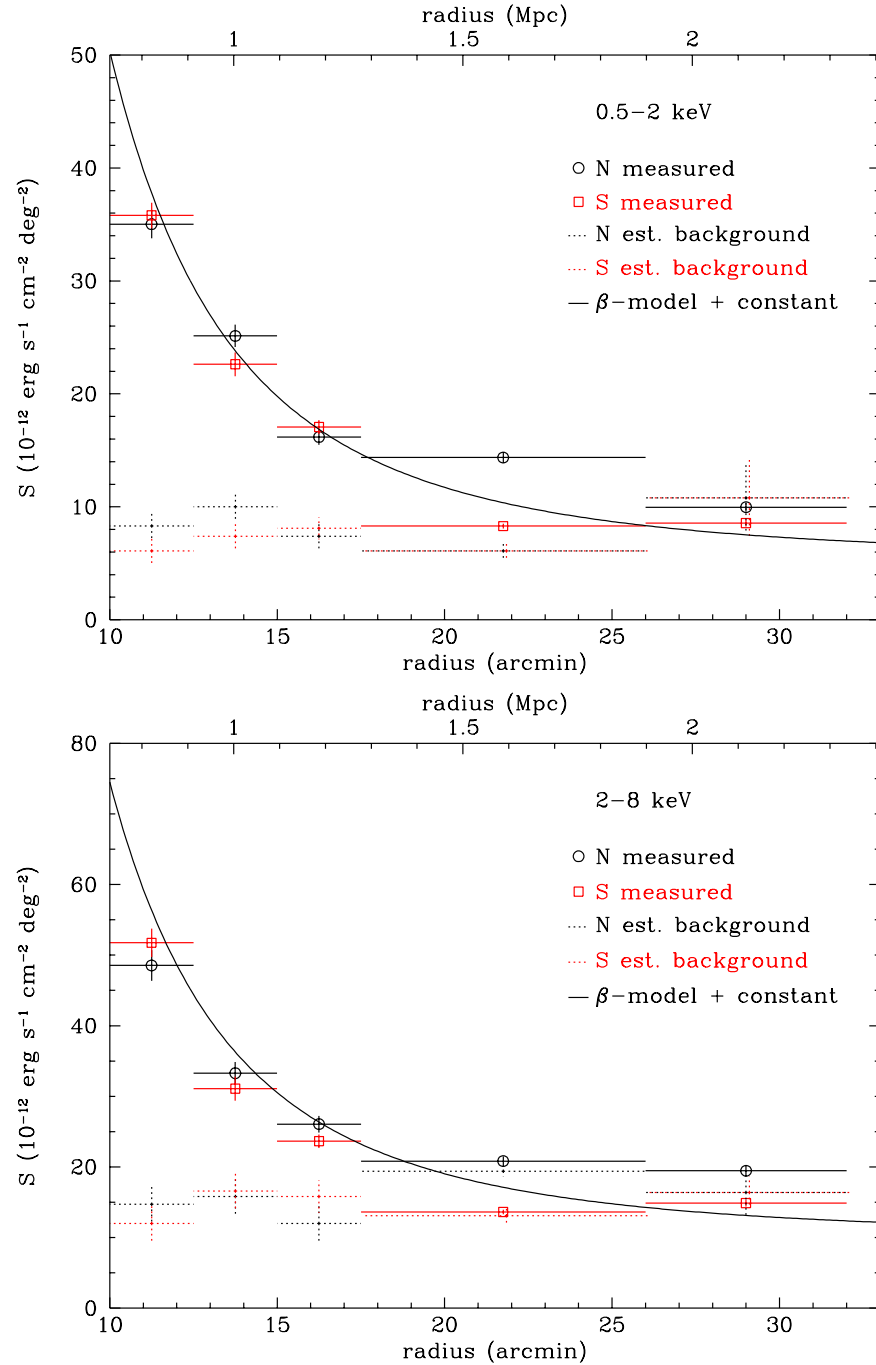


Fig. 9. Surface brightness profiles at large radius in the 0.5–2 keV (top) and 2–8 keV (bottom) bands. Profiles running northward (black circles) and southward (red squares) from the cluster center, with estimated corresponding background levels (dashed histograms; black to north, red to south) are shown. The solid curves are the best-fit β -models assuming a spatially constant background. The cluster surface brightness data have been rebinned to match the spectral extraction regions; the models are identical to those shown in Figure 8. The background estimates account for point sources detected by XMM-Newton but unresolved by Suzaku, and assume no SWCX emission (see text).

counts (Moretti et al. 2003). The latter two components are listed for each spectral analysis region in Table 5. Error bars plotted on the background histograms include the expected RMS Poisson fluctuations, also as listed in Table 5. The global best-fit β -models (assuming a spatially uniform background) are shown as solid curves in Figure 9.

Figure 9 shows that the background model agrees well with the measured surface brightness in the background regions (at $r > 26'$), which suggests that our extragalactic background model is reasonable. In the region $17.5' < r < 26'$ ($1.3 < r < 1.9$ Mpc; $r_{500} < r < r_{200}$), the observed soft-band emission significantly exceeds the background in both the north and the south. The formal net soft-band cluster surface brightnesses in this radial range are $B_{cl} = 8.3 \pm 0.8$ (2.2 ± 0.6) $\times 10^{-12}$ erg s $^{-1}$ cm $^{-2}$ deg $^{-2}$ in the north (south), quoting 1σ errors. Allowing for scattered flux contributions listed in Table 4, the north detection is significant at a level greater than 8σ ; the net cluster surface brightness in the south falls below 3σ .

If we allow for possible SWCX contributions, the estimated Galactic plus geocoronal background is somewhat higher, but we still find significant cluster emission in the north. In this case, the estimated Galactic plus geocoronal background rises to $B_{Gal+SWCX} = 4.3 \pm 0.5$ (4.1 ± 0.5) $\times 10^{-12}$ erg s $^{-1}$ cm $^{-2}$ deg $^{-2}$ in the north (south), with 1σ errors. The corresponding results for cluster flux are $B_{cl} = 7.0 \pm 0.8$ (1.1 ± 0.6) $\times 10^{-12}$ erg s $^{-1}$ cm $^{-2}$ deg $^{-2}$ in the north (south), with 1σ errors. In the north, the signal exceeds the background by at least 6.8σ , allowing for the scattered light contributions listed in Table 4. The 3σ upper limit on the cluster emission in the south is $B_{cl} < 1.8 \times 10^{-12}$ erg s $^{-1}$ cm $^{-2}$ deg $^{-2}$.

We also note that formally the measured net cluster surface brightness in the north exceeds that in the south by a factor of 6.4 ± 3.6 (1σ error); the absolute brightness difference of $5.9 \pm 1.1 \times 10^{-12}$ erg s $^{-1}$ cm $^{-2}$ deg $^{-2}$ is significant at more than 5.3σ . We conclude that Suzaku has detected soft-band cluster emission with high confidence in a region with $r_{500} < r < r_{200}$ north of the cluster center, but not in the corresponding region in the south. In this radial range, the cluster is significantly brighter in the north than in the south.

The lower panel of Figure 9 shows that Suzaku detects no hard-band cluster emission at $r > 17.5'$ (1.3 Mpc) in either north or south. Indeed, the Suzaku surface brightness measurements are remarkably consistent with the background estimates derived from the XMM-Newton point-source catalog and the assumed number-counts model for $17.5' < r < 26'$. In the hard band, the significant north-south difference in measured Suzaku surface brightness is attributable entirely to differences in the background source populations in these two regions.

Finally, comparison of the top and bottom panels of Figure 9 shows that our background model implies spatial variations in the spectral shape of the background. For example, the background is marginally harder in the north than in the south in the radial range $17.5' < r < 26'$, and in the north the background is harder at $17.5' < r < 26'$ than

Table 6. Power-law fits to surface brightness profiles

Direction	Index ^a	
	0.5–2 keV	2–8 keV
<i>r</i> > 7.5'		
N	2.63 ^{+0.32} _{-0.31}	3.79 ^{+0.44} _{-0.38}
S	3.43 ^{+0.29} _{-0.28}	4.06 ^{+0.45} _{-0.40}
N+S	2.98 ^{+0.21} _{-0.20}	3.85 ^{+0.31} _{-0.29}
7.5' < <i>r</i> < 17.5'		
N	3.10 ^{+0.36} _{-0.36}	3.51 ^{+0.51} _{-0.47}
S	3.30 ^{+0.33} _{-0.32}	3.88 ^{+0.48} _{-0.44}
N+S	3.20 ^{+0.24} _{-0.24}	3.68 ^{+0.34} _{-0.32}

Notes:

^a Index α in $S(r) \propto r^{-\alpha}$, with 90% errors.

at $r > 26'$. We allow for these variations in the spectral fitting used to extract the temperature profiles discussed below.

Simulations of cluster X-ray emission in the vicinity of the virial radius (Roncarelli et al. 2006) suggest that the surface brightness profile follows a broken power law with the break at $r \approx r_{200}$. Simple power-law fits to the A1795 surface brightness profiles at $r < r_{200}$ are roughly consistent with these simulations. Best-fit values for the power-law index α , where $S(r) \propto r^{-\alpha}$, are listed in Table 6. The two different radial ranges shown correspond to $r > 0.3r_{200}$ ($r > 7.5'$) and $0.3r_{200} < r < 0.7r_{200}$ ($7.5' < r < 17.5'$). In the soft band, the northern and southern profile slopes are identical, within errors, over the smaller radial range, but the apparent excess emission at $r > 0.7r_{200}$ ($r > 17.5'$) flattens the profile there. In all cases the hard-band profile slopes are steeper than the corresponding soft-band slopes.

The soft-band power-law index for the southern profile is quite similar to that reported by Neumann (2005) from stacked ROSAT profiles for a number of hot clusters. For example, Neumann finds $\alpha = 3.79^{+0.39}_{-0.37}$ for $0.3r_{200} < r < 1.2r_{200}$ for a set of clusters similar to (and including) A1795. On the other hand, the soft-band Suzaku profile north of the cluster center is somewhat shallower than the stacked ROSAT profile.

We have fit the rolling power-law function used by Roncarelli et al. (2006) to our data. This function is $S(x) \propto x^{-\gamma(x)}$ with $x \equiv r/r_{200}$ and $\gamma(x) \equiv -(b_{max}x + b_{min})/(1+x)$. At small r , $S(x) \rightarrow x^{-b_{min}}$, while at large r , $S(x) \rightarrow x^{-b_{max}}$, with the transition occurring around $x \sim 1$. Our data are confined to $x \lesssim 1$, so they do not constrain b_{max} well. Therefore in our fits we fix $b_{max} = 5.3$ (7.5) for the soft (hard) band, values typical of the simulated clusters (Roncarelli et al. 2006). With these constraints we find $b_{min} = 2.6$ – 3.5 , consistent with the simulations, for both hard-band profiles and for the soft-band profile in the south. Again because of the excess emission at $r > 17.5'$ in the north, however, we find $b_{min} \approx 2.2$ for the soft-band profile in this direction; this is flatter than the simulated clusters.

We note that Roncarelli et al. (2006) filter the emission

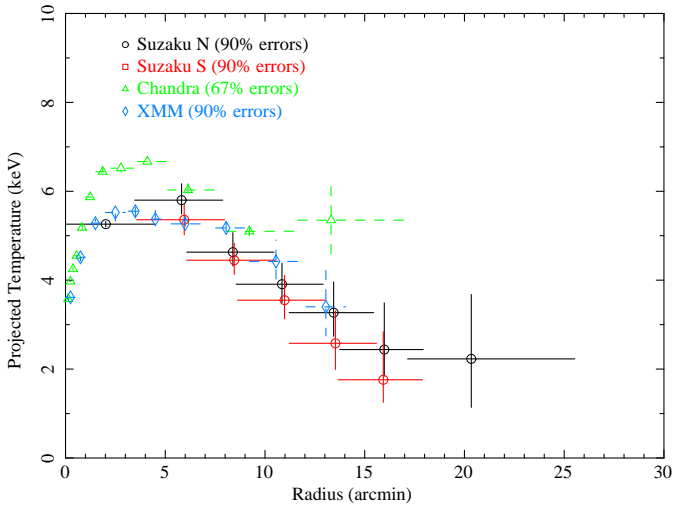


Fig. 10. Projected temperature profiles running northward (black circles) and southward (red squares) from the cluster center. Data from Chandra (green triangles; Vikhlinin et al. 2006) and XMM-Newton (blue diamonds; Snowden et al. 2008; Snowden, private communication) are also shown. The radius values for the Suzaku data reflect the average originating radius of photons detected in each extraction region, as described in Section 4.2. Likewise, the horizontal Suzaku error bars indicate 90% confidence for originating location of detected photons. The error bars for other missions indicate the radial range of the bin.

from their simulated clusters before extracting surface-brightness and temperature profiles. The aim of this filtering is to remove high-density, low-temperature features which are presumed to be too faint to detect, or perhaps even non-physical artifacts of the simulations. We note that profiles of unfiltered, individual simulated clusters (see, for example, their Figure 2) show significant departures from the filtered soft-band surface brightness profile, especially at $r > 0.5r_{200}$. The magnitude of these deviations is at least as great as the north-south difference we see in Abell 1795. Similar fluctuations are not seen in the hard-band profiles of the simulated clusters. We conclude that the north-south surface brightness difference we observe is similar to features present in these (unfiltered) simulated clusters.

4.2. Temperature, Density and Entropy Profiles

The temperature profiles to the north and south of the cluster are shown in Figure 10, along with results from Chandra and XMM-Newton. We are able to measure the cluster temperature past the limit of XMM-Newton and Chandra data (about 1.1 Mpc or $15'$) and find that the temperature continues to decline to the largest radius at which emission is detectable. At the outermost radial bin, spanning $1.3 < r < 1.9$ Mpc, the temperature is about one-third of the peak cluster temperature observed by Suzaku.

The radial values and 90% error bars shown in Figure 10 are estimated from the `xissimarfgen` ray-tracing simulations described in Section 2.3.1. These radial bins more accurately reflect the real locations of photons originating from the cluster, and we use these values for the profile

fitting described in the remainder of this section. Such corrections are less straightforward for the surface brightness profiles shown in Figures 8 and 9, since the emission in that case is from a combination of sources (i.e., cluster and cosmic background) that have different spatial distributions.

The Suzaku data do not resolve the cool core at $r < 2'$, but at larger radii we find good agreement between the Suzaku and XMM-Newton in the radial range covered by both observatories. Note that here we have used the most recent analysis of the XMM-Newton data by Snowden (private communication), which uses the latest EPIC-pn calibrations and provides somewhat lower temperatures than those reported earlier (Piffaretti et al. 2005; Snowden et al. 2008). The Chandra temperatures reported by Vikhlinin et al. (2006), however, are generally higher than the Suzaku (and XMM-Newton) temperatures outside the cool core, especially at $r < 7.5'$. The reason for this discrepancy is not entirely clear. In principle, scattering by the telescope of photons from the bright, cool core over the central few arcminutes would tend to reduce the apparent temperature. One might expect the scattering to be more significant for Suzaku, and, to a lesser extent, for XMM-Newton than for Chandra, given the latter's much sharper point response function. If this effect were important at radii as large as $r = 7.5'$, however, it would be surprising if Suzaku and XMM-Newton data agreed as well as they do, given their very different point response characteristics. A more plausible explanation may lie in the known discrepancy between Chandra and XMM-Newton temperatures for relatively hot ($kT > 4$ keV) clusters.⁷ Chandra reports temperatures that are systematically higher than those from XMM-Newton for such clusters, and the magnitude of the discrepancy at $kT_{XMM} \sim 5$ keV is very close to that shown in Figure 10 at $r = 5'$. The discrepancy is smaller at lower temperatures. Uncertainties in the thickness of a thin (~ 10 – 20 Å) contamination layer on the Chandra mirrors likely account for this discrepancy. We note that this effect is unlikely to explain the discrepancy at $r > 12'$, where $kT_{XMM} \approx 4$ keV, a temperature at which this calibration error is thought to be quite small. We also note that the azimuthal range covered by the Chandra observations (Vikhlinin et al. 2005) differs from that we observed with Suzaku at these large radii. In principle, therefore, the discrepancy between Chandra and Suzaku results at this large radius could reflect azimuthal temperature variations in the cluster. In any event, we are principally concerned here with the cluster temperature profile at $r > 5'$. Given the good agreement between the Suzaku and XMM-Newton temperature profiles in this radial range, we base our subsequent analysis on the Suzaku temperatures shown in Figure 10.

Fitting a power law (assuming $T \propto r^{-\gamma}$) to the projected temperature at $r > 7.5'$ yields consistent slopes in the north and the south, and $\gamma = 0.9 \pm 0.3$ for a joint fit to all the data in this radial range. This is similar to the

⁷ L. David, 2007, http://cxc.harvard.edu/ccw/proceedings/07_proc/presentations/david/

value $\gamma = 0.98 \pm 0.07$ reported by George et al. (2008) from Suzaku observations of the outskirts of the cluster around PKS 0745-191.

We deprojected the temperature profiles to the north and south of the cluster separately using the `smaug` model in `XSPEC`. The `smaug` algorithm (Pizzolato et al. 2003) fits analytic functions for the deprojected temperature, density, and abundance profiles, and compares the reprojected spectra to the data. We fit spectra in the radial range 5–17.5′ (0.37–1.28 Mpc), although the profiles were extended to 2 Mpc for reprojection. Since the emission north of 17.5′ is evidently not part of a spherically symmetric component, we excluded it from the deprojection. We assumed profiles of the form $f = f_0[1 + (r/r_c)^2]^{-\epsilon}$, where f_0 , r_c and ϵ were allowed to vary independently for the temperature and density profiles, while f_0 and ϵ were allowed to vary for the abundance profile. The abundance profile r_c parameter was frozen at 10 kpc, essentially producing a power-law dependence over the fitting region. We assumed a `mekal` model for the plasma emission, and included Galactic and extragalactic components identical to those described in Section 2. Parameter errors were estimated using MCMC techniques identical to those described in Section 2.3.3.

The best-fit deprojected power-law temperature profiles are shown as continuous curves in Figure 11, along with the measured (projected) temperatures. The shaded regions surrounding the curves indicate 90% confidence intervals. The best-fit model parameters for deprojected temperature, hydrogen density, and abundance profiles are listed in Table 7. Figure 11 shows that the model deprojected temperatures track the observed projected temperatures quite closely. As expected, the deprojected temperatures are slightly higher, but, as suggested by George et al. (2008), the difference is relatively small, especially at large radius. Note that formally the fit quality is acceptable in the south but marginal in the north (see Table 7).

As expected from the projected temperatures (see Figure 10), the deprojected Suzaku temperatures are somewhat lower than those inferred from Chandra data (Vikhlinin et al. 2006). Moreover, our deprojected temperature profile falls more rapidly with increasing radius than does the Chandra profile. For example, at $r = 1.3 \text{ Mpc} \approx r_{500}$, our (average) model profile has a logarithmic slope $-d \ln T / d \ln r \equiv \gamma = 0.77^{+0.16}_{-0.09}$ while Vikhlinin et al. (2006) find $\gamma = 0.48 \pm 0.15$. (Here we cite 68% confidence errors.) In interpreting this comparison one must again bear in mind that the Suzaku and Chandra observations sample different ranges in azimuth around the cluster. Our measured slope is also steeper than those found for simulated clusters by both Hallman et al. (2007), who fit a functional form with logarithmic slope $\gamma \sim 0.4 \pm 0.2$ at $r = r_{500}$, and by Roncarelli et al. (2006), who report $\gamma \sim 0.4\text{--}0.6$ at $r < r_{200}$. In the latter case the steeper slope is associated with simulations which include radiative cooling.

Our deprojected density profile approaches a power law at large radius, and the results in Table 7 imply $-d \ln n_H / d \ln r \equiv \alpha = 2.27 \pm 0.07$ at $r = 1.3 \text{ Mpc}$. This

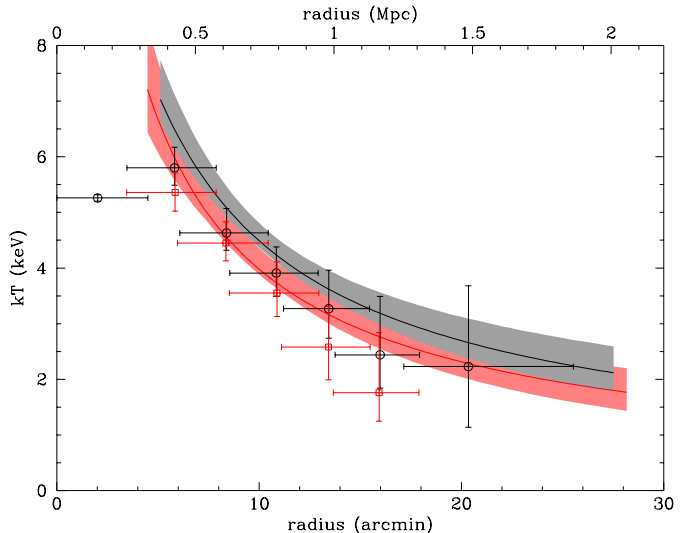


Fig. 11. Deprojected temperature profiles (solid lines) and 90% confidence intervals (shaded regions) plotted with the observed projected temperatures from Figure 10 (points). Results for the north are in black, those for the south are in red. Only the annuli between 5–17.5′ were included in the deprojection.

is in agreement with the density profile slope reported by Vikhlinin et al. (2006) from Chandra data: their fitting formula is reasonably well-approximated by a power law with index $\alpha = 2.21$ over the radial range we consider. Our assumed forms for density and temperature imply that the ICM should be polytropic at large radius, with a best-fit index of $\Gamma = 1.3^{+0.3}_{-0.2}$.

Finally, we have computed the implied entropy index, ($s \equiv kT/n_e^{2/3}$) as a function of radius, assuming $n_e = 1.2 \times n_H$. The result is shown, with 90%-confidence uncertainties, in Figure 12. There we also show the entropy profile expected from hierarchical structure formation derived from (non-radiative) simulations by Voit (2005); this curve increases as $s \sim r^{1.1}$. Our average entropy profile increases more slowly, as $s \sim r^{0.74 \pm 0.20}$.

The relatively low temperatures and entropies we observe in the outskirts of Abell 1795 may be an indication that the plasma we detect is not in hydrostatic equilibrium in the cluster’s gravitational potential. We note that our Suzaku observations sample two restricted sectors of the cluster at this radius, and that data from other observatories sample different sectors. If the ICM is not in hydrostatic equilibrium at this radius, one might expect azimuthal variations in ICM density and temperature. For example, as we noted earlier in Section 4.1, the simulations of Roncarelli et al. (2006) produce (unfiltered) clusters with distinct cool clumps at $r < r_{200}$. These may be the result of relatively cool, low-mass substructures falling toward the cluster center. Moreover, Mahdavi et al. (2008) infer modest departures from hydrostatic equilibrium at radii $r_{2500} < r < r_{500}$ from a comparison of cluster masses determined from X-ray and weak-lensing data. This result is at least qualitatively in agreement with our interpretation of the temperature and entropy profiles of Abell 1795.

Table 7. Best-fit Parameters for Deprojected Profiles^a

		north	south	average
kT	f_0 (keV)	$12.8^{+1.1}_{-0.9}$	$16.2^{+1.7}_{-1.3}$	$14.5^{+1.4}_{-1.1}$
	ϵ	$0.38^{+0.12}_{-0.09}$	$0.40^{+0.12}_{-0.10}$	$0.39^{+0.12}_{-0.09}$
	r_c (Mpc)	$0.19^{+0.10}_{-0.06}$	$0.13^{+0.09}_{-0.05}$	$0.16^{+0.10}_{-0.05}$
n_H	f_0 (10^{-3} cm $^{-3}$)	$3.03^{+0.10}_{-0.08}$	$3.06^{+0.11}_{-0.09}$	$3.04^{+0.11}_{-0.08}$
	ϵ	$1.17^{+0.03}_{-0.03}$	$1.22^{+0.03}_{-0.03}$	$1.20^{+0.03}_{-0.03}$
	r_c (Mpc)	$0.30^{+0.01}_{-0.01}$	$0.30^{+0.01}_{-0.01}$	$0.30^{+0.01}_{-0.01}$
abund	f_0 (solar)	$4.31^{+0.27}_{-3.02}$	$4.40^{+0.19}_{-2.91}$	$4.36^{+0.24}_{-2.97}$
	ϵ	$0.36^{+0.05}_{-0.14}$	$0.36^{+0.06}_{-0.12}$	$0.36^{+0.06}_{-0.13}$
	r_c (Mpc) ^b	0.01	0.01	0.01
χ^2/dof		1875.93/1686	1851.83/1810	...

^a Profiles are of the form $f = f_0[1 + (r/r_c)^2]^{-\epsilon}$

^b The abundance core radius was fixed.

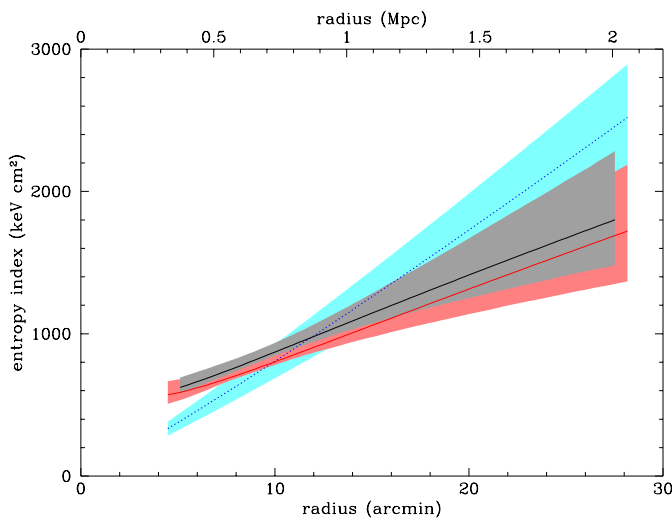


Fig. 12. Entropy profiles (solid lines) and 90% confidence intervals (shaded regions). Results for the north are in black, those for the south are in red. Plotted is the entropy index $s = kTn_e^{-2/3}$ in keV cm 2 . Only annuli between 5–17.5' were used in the deprojection to determine the profiles. The blue line and shaded region are from simulations reported by Voit (2005) for non-radiative, hierarchical cluster formation.

4.3. Cluster Mass

The X-ray surface brightness and temperature profiles can be used to estimate the cluster mass as a function of radius if we assume that the ICM is hydrostatic equilibrium. In this case, following Vikhlinin et al. (2006),

$$M(< r) = -3.68 \times 10^{13} M_\odot \left[\frac{T(r)}{1 \text{ keV}} \right] \left[\frac{r}{1 \text{ Mpc}} \right] \times \left[\frac{d \log \rho_g}{d \log r} + \frac{d \log T}{d \log r} \right]. \quad (1)$$

Here ρ_g is the mass density of the ICM and it is assumed that the mean molecular weight of the ICM $\mu = 0.62$. Chandra (Vikhlinin et al. 2006) and XMM-Newton (Ikebe et al. 2004; Piffaretti et al. 2005) have been used to estimate mass profiles for Abell 1795 at radii up to $r \lesssim 1.3$

Mpc. In this section we compare mass constraints obtained from our Suzaku observations with these measurements.

Adopting the mean of the north and south profiles for the deprojected temperature and density (see Table 7), together with the mean of the north and south temperatures measured in the final radial bin of each deprojected profile, we use Equation 1 to estimate the cluster mass. We obtain $M = 4.1^{+0.5}_{-0.3} \times 10^{14} M_\odot$ within $r = 1.27$ Mpc, the value of r_{500} reported by Vikhlinin et al. (2006). The 68% confidence uncertainties quoted here are dominated by uncertainties in the temperature measurement.

Our mass estimate is somewhat lower than others reported for Abell 1795. Vikhlinin et al. (2006) find $M = 6.0 \pm 0.5 \times 10^{14} M_\odot$ at $r = 1.27$ Mpc, while Piffaretti et al. (2005) report $M = 5.2 \pm 0.4 \times 10^{14} M_\odot$ at $r = 1.16$ Mpc. Formally, these exceed our mass estimate by 2.7σ and 1.7σ , respectively. The discrepancy is almost entirely due to the difference in temperature estimated at these radii. For example, the best-fit model used by Vikhlinin et al. (2006) for the deprojected temperature predicts $T = 3.8$ keV, while we estimate $T = 2.9^{+0.3}_{-0.1}$ keV at $r = 1.27$ Mpc.

Our lower mass estimate implies $r_{500} = 1.08^{+0.07}_{-0.03}$ Mpc, somewhat smaller than the Chandra estimate of $r_{500} = 1.27 \pm 0.04$ Mpc (Vikhlinin et al. 2006), and consistent with the XMM-Newton value $r_{500} = 1.16 \pm 0.05$ Mpc (Piffaretti et al. 2005). Similarly, we find $r_{200} = 1.52^{+0.10}_{-0.07}$ Mpc, smaller than both the Beppo-Sax estimate of $r_{200} = 2.14 \pm 0.46$ (Ettori, De Grandi & Molendi 2002), and the value ($r_{200} = 1.9$ Mpc) we estimate from theoretical scaling relations (Evrard, Metzler & Navarro 1996; Arnaud & Evrard 1999). Finally, given that $r_v \approx r_{100}$ in our assumed cosmology (Bryan & Norman 1998), our mass profile implies $r_v = 2.0$ Mpc.

The rapidly falling temperature profile we observe implies a rapidly falling mass density profile and a slowly rising integrated mass profile (see Equation 1). A power-law approximation to our best-fit integrated mass profile in the region $1 < r < 2$ Mpc yields $M(< r) = 3.7 \times 10^{14} M_\odot \left(\frac{r}{1 \text{ Mpc}} \right)^{0.24}$. This is much flatter, for example, than the slope expected from an NFW model with scale

radius $r_s = 0.385$ Mpc reported by Vikhlinin et al. (2006).

5. Summary and Conclusions

We have presented results of Suzaku observations of two distinct regions in the outskirts of Abell 1795. We detect X-ray emission to $r = 1.3$ Mpc in both regions, and in the north trace the hot ICM to $r = 1.9$ Mpc $\geq r_{200}$. We find that the X-ray surface brightness at $1.3 < r < 1.9$ Mpc is significantly higher in the north than in the south. We measure the run of temperature with radius at $r > r_{2500}$ and find that it falls relatively rapidly ($T_{deprojected} \propto r^{-0.9}$) and reaches a value about one-third of its peak at the cluster outskirts.

One possible interpretation of our observations is that the ICM is not in hydrostatic equilibrium in the radial range $r_{500} < r < r_{200}$, and that in the north we are seeing infalling plasma at relatively low ($kT \sim 2$ keV) temperature. In support of this picture we note that the X-ray surface brightness is neither azimuthally symmetric nor (in the north) falling monotonically with increasing radius. Moreover, the rapidly falling deprojected temperature profile would require that there is relatively little gravitating mass at $r > 1.3$ Mpc if the ICM is polytropic and in hydrostatic equilibrium, a result that conflicts with extrapolations of the best-fit NFW profiles derived from high-resolution Chandra observations (Vikhlinin et al. 2006).

Simulations (Roncarelli et al. 2006) predict, and recent lensing and X-ray observations (Mahdavi et al. 2008; George et al. 2008) provide evidence for, modest deviations from hydrostatic equilibrium in the ICM at $r_{2500} < r < r_{200}$. Our observations of Abell 1795 suggest that in some cases these deviations may be quite significant even in a cluster which appears to be relaxed at smaller radii. Additional observations of a variety of clusters, with more complete azimuthal coverage than we have obtained, will improve understanding of the state of the ICM in cluster outskirts, and therefore of cluster masses, structure and formation mechanisms.

Finally, we note that these and other observations of the low-surface-brightness outskirts of clusters have been made possible by Suzaku's relatively low and stable non-X-ray background. The surface brightness sensitivity of our observations, $B_{0.5-2\text{keV}} > 1.8 \times 10^{-12}$ erg s $^{-1}$ cm $^{-2}$ deg $^{-2}$ (3σ), is less than 20% of the total cosmic background in this spectral band. Our sensitivity was ultimately limited by time-variable solar wind charge exchange emission and by Poisson variations in the extragalactic source density. We demonstrated here that variations in the geocoronal contribution can be modeled to this level from simultaneous observations of cluster-free background regions. To reduce background source density variations below this level in the relatively small cluster regions ($0.01-0.03$ deg 2) we required information from the XMM-Newton source catalog. Future Suzaku observations of cluster outskirts would benefit from coverage of larger (~ 0.1 deg 2) solid angle in each radial bin, especially if deep X-ray source catalogs are not available.

Acknowledgements

We thank Alexey Vikhlinin and Steve Snowden for providing temperature data from Chandra and XMM-Newton, respectively, and Helen Russell for useful discussions about deprojection. MWB and EDM were supported in part by NASA grant NNG05GM92G to MIT. J.P. Hughes acknowledges support from NASA grant NNGG05GP87G. J.P. Henry acknowledges support from NASA grant NNG06GC04G.

References

- Anders, E., & Grevesse, N. 1989, *Geochim. Cosmochim. Acta*, 53, 197
- Arnaud, K. A. 1996, in *Astronomical Data Analysis Software and Systems V*, ed Jacoby, G., & Barnes, J., ASP Conference Series volume 101, p17
- Arnaud, M., & Evrard, A. 1999, *MNRAS*, 305, 631
- Böhringer, H., et al. 2000, *ApJS*, 129, 435
- Borgani, S., et al. 2004, *MNRAS*, 348, 1078
- Brandt, W. N., & Hasinger, G. 2005, *ARA&A*, 43, 827
- Bryan, G., & Norman, M. 1998, *ApJ*, 495, 80
- Carter, J. A., & Sembay, S. 2008, *A&A*, 489, 837
- Cravens, T. E. 2000, *ApJL*, 532, L153
- DeLuca, A., & Molendi, S. 2004, *A&A*, 419, 837
- Dickey, J. M., & Lockman, F. J. 1990, *ARA&A*, 28, 215
- Ettori, S., & Balestra, I. 2008, *A&A*, in press (astro-ph/0811.3556)
- Ettori, S., De Grandi, S., & Molendi, S. 2002, *A&A*, 391, 841
- Evrard, A., Metzler, C., & Navarro, J. 1996, *ApJ*, 469, 494
- Fabian, A. C., Sanders, J. S., Ettori, S., Taylor, G. B., Allen, S. W., Crawford, C. S., Iwasawa, K., & Johnstone, R. M. 2001, *MNRAS*, 321, L33
- Fujita, Y., Tawa, N., Hayashida, K., Takizawa, M., Matsumoto, H., Okabe, N., & Reiprich, T. 2008, *PASJ*, 60, S343
- Fujimoto, R., et al. 2007, *PASJ*, 59, S133
- George, M., Fabian, A., Sanders, J., Young, A. & Russell, H. 2008, *MNRAS*, 395, 657 (astro-ph/0807.1130)
- Hallman, E., Burns, J., Motl, P., & Norman, M. 2007, *ApJ*, 665, 911
- Horner, D. 2001, PhD Thesis, University of Maryland
- Ikebe, Y., Böhringer, H., & Kitayama, T. 2004, *ApJ*, 611, 175
- Ishisaki, Y. et al. 2007, *PASJ*, 59, S113
- Kalberla, P. M. W., Burton, W. B., Hartmann, D., Arnal, E. M., Bajaja, E., Morras, R., & Pöppel, W. G. L. 2005, *A&A*, 440, 775
- Koutroumpa, D., Acero, F., Lallement, R., Ballet, J., & Kharchenko, V. 2007, *A&A*, 475, 901
- Koyama, K., et al. 2007, *PASJ*, 59, S23
- Kuntz, K., & Snowden, S. 2000, *ApJ*, 543, 195
- Mahdavi, A., Hoekstra, H., Babul, A., & Henry, J. P. 2008, *MNRAS*, 384, 1567
- Miller, E. D., et al. 2008, *PASJ*, 60, S95
- Moretti, A., Campana, S., Lazzati, D., & Tagliaferri, G. 2003, *ApJ*, 588, 696
- Navarro, J., Frenk, C., & White, S. 1997, *ApJ*, 490, 493
- Neumann, D. 2005, *A&A*, 439, 465
- Piffaretti, R., Jetzer, Ph., Kaastra, J., & Tamura, T. 2005, *A&A*, 433, 101
- Pizzolato, F., Molendi, S., Ghizzardi, S., & De Grandi, S. 2003, *ApJ*, 592, 62

- Reiprich, T. H., Hudson, D. S., Zhang, Y.-Y., Sato, K.,
Ishisaki, Y., Hoshino, A., Ohashi, T., Ota, N., & Fujita,
Y. 2008, *A&A*, accepted (arXiv:0806.2920)
- Roncarelli, M., Ettori, S., Dolag, K., Moscardini, L., Borgani,
S., & Murante, G. 2006, *MNRAS*, 373, 1339
- Serlemitsos, P. et al. 2007, *PASJ*, 59, S9
- Smith, R., et al. 2004, *AJ*, 128, 1558
- Snowden, S., Egger, R., Freyberg, M., McCammon, D.,
Plucinsky, P., Sanders, W., Schmitt, W., & Trümper, J.
1997, *ApJ*, 485, 125
- Snowden, S. L., Collier, M. R., & Kuntz, K. D. 2004, *ApJ*,
610, 1182
- Snowden, S., Mushotzky, R., Kuntz, K., & Davis, D. 2008,
A&A, 478, 615
- Stone, E. C., Frandsen, A. M., Mewaldt, R. A., Christian,
E. R., Margolies, D., Ormes, J. F., & Snow, F. 1998, *Space
Science Reviews*, 86, 1
- Tawa, N., et al. 2008, *PASJ*, 60, S11
- Vikhlinin, A., Markevitch, M., Murray, S. S., Jones, C.,
Forman, W., & Van Speybroeck, L. 2005, *ApJ*, 628, 655
- Vikhlinin, A., Kravtsov, A., Forman, W., Jones, C.,
Markevitch, M., Murray, S. S., & Van Speybroeck, L. 2006,
ApJ, 640, 691
- Vikhlinin, A., Forman, W., & Jones, C. 2003, *ApJ*, 525, 47
- Voit, M. 2005, *Rev. Mod. Phys.*, 77, 207
- Watson, M., et al. 2001, *A&A*, 365, L59
- Yang, Y., Mushotzky, R., Barger, A., Cowie, L., Sanders, D.,
& Steffen, A. 2003, *ApJ*, 585, L85